

Inclusion of Anion Additives in the Inner Solvation Shell to Regulate the Composition of Solid Electrolyte Interphase

Harshita Lohani, Ajit Kumar, Amreen Bano, Arpita Ghosh, Pratima Kumari, Aakash Ahuja, Abhinanda Sengupta, Dhruv Kumar, Dan Thomas Major, and Sagar Mitra*

An innovative approach to electrolyte engineering in carbonate electrolytes is introduced by incorporating high donor number dual anion additives into the conventional electrolyte system (1 M NaPF₆ EC:PC). The active engagement of anions in the primary solvation shell effectively hinders the reduction of solvent molecules by reducing the Lowest Unoccupied Molecular Orbital (LUMO) of Na⁺-solvent-anion complex as compared to the LUMO of pure solvents or Na⁺-solvent complex. The participation of anions leads to the formation of a thinner and an inorganic-rich Solid Electrolyte Interphase on the hard carbon anode enhancing Initial Coulombic Efficiency and significantly improving its kinetics. Moreover, the system with dual anion additives exhibits oxidative stability up to 4.5 V, effectively mitigating the undesired side reactions at high voltage operation of the layered sodium nickel manganese oxide cathode. The addition of dual anion additives proves instrumental in suppressing structural degradation and transition metal dissolution during the long cycling performance of the layered oxide cathode in a sodium-ion full cell. The synergistic effects of this dual anion additive added electrolyte on both the anode and the cathode ultimately ensured prolonged cycling of the sodium-ion full cell. The electrolyte engineering approach outlined in this study opens the door to advancing next-generation high-voltage sodium batteries.

sodium resources, lower cost, and reduced environmental impact, making them a compelling solution for scalable and sustainable energy storage systems. However, despite their considerable potential, several challenges, such as suboptimal cycling stability in full cells^[1] and inadequate kinetics between electrodes and electrolytes,^[2] impede the seamless commercialization of NIBs.

The main obstacles hindering the successful commercialization of NIBs, utilizing a hard carbon (HC) anode and a high-voltage cathode, lie in the challenges associated with low initial coulombic efficiency (ICE)^[3] and the formation of an unstable solid electrolyte interphase (SEI) on the surface of the HC anode^[4] and the cathode electrolyte interphase (CEI) on the high-voltage cathode,^[5] respectively. The composition of the SEI layer developed on the HC anode surface predominantly consists of porous organic components, primarily originating from the decomposition of solvents within the electrolyte.^[6] This composition adversely influences the chemical and mechanical stability of the SEI layer, thereby impacting the long-term cycling stability of sodium batteries.^[1] Additionally, an unstable CEI has been identified as a constraint on the high-voltage operation of the cathode.^[5] This

1. Introduction

Sodium-ion batteries (NIBs) hold great promise as the next-generation energy storage system due to their abundance of

H. Lohani, P. Kumari, A. Ahuja, A. Sengupta, S. Mitra
 Electrochemical Energy Laboratory
 Department of Energy Science and Engineering
 Indian Institute of Technology Bombay
 Mumbai 400076, India
 E-mail: sagar.mitra@iitb.ac.in

A. Kumar
 Institute for Frontier Materials
 Melbourne Burwood Campus
 DEAKIN University
 Burwood 3125, Australia

 The ORCID identification number(s) for the author(s) of this article can be found under <https://doi.org/10.1002/aenm.202401268>

DOI: 10.1002/aenm.202401268

A. Bano, D. T. Major
 Department of Chemistry and Institute of Nanotechnology and Advanced Material
 Bar-Ilan University
 Ramat Gan 5290002, Israel
 A. Ghosh
 ICGM
 CNRS
 ENSCM
 Université Montpellier
 Montpellier Cedex 5 34095, France
 D. Kumar
 Vellore Institute of Technology
 Vellore 632014, India

instability of CEI causes the continuous decomposition of the electrolyte, leading to the dissolution of transition metals in oxide-based cathodes under high-voltage operation.^[5] Recently, various investigations have presented methodologies to enhance both ICE^[7] and methods to extend the cycling performance of sodium full cells.^[8–10] These approaches include the chemical^[11,12] or electrochemical^[13] presodiation of HC, the incorporation of film-forming additives,^[14] the creation of an artificial SEI on the surface of the HC anode,^[15] the formation of a stable CEI on the surface of the cathode through electrolyte engineering^[16] and the application of protective coatings^[17,18] on both anode and cathode.

Among these methods, manipulating the solvation structure around the Na^+ cation through electrolyte engineering emerges as the most straightforward and efficient method to modulate the interphase formation on both the anode and cathode, subsequently enhancing the ICE and cycling stability of sodium batteries.^[19,20] Nevertheless, most of these studies have primarily concentrated on incorporating fluorinated solvents^[21,22] as an additive or employing ether-based solvents.^[23] However, it is noteworthy that these solvents face limitations in high-voltage and high-temperature battery applications due to concerns related to anodic stability and inadequate thermal stability.^[24] In the context of LIB research, it has been shown that the participation of anions in the inner solvation structure can weaken the cation-solvent coordination and thus induce the preferential reduction of anion by enhancing its reduction potential during single electron reduction^[25] ultimately leading to the formation of anion rich interphases in lithium batteries. However, within the realm of NIB research, a notable need exists for studies exploring the use of anions as additives to enhance the extended cycling performance of sodium full cells.

This study focuses on delving into the solvation structure to comprehend the interactions and conformations of Na^+ -solvent and Na^+ -solvent-anion complexes by adding 2 high-donor salt anions as additives. Introducing high-donor salt anions enables a robust binding with Na^+ cations, compelling cations to draw electrons from donor anions and facilitating additive anions' involvement in the reduction process for forming SEI. We have also explored the impact of dual anion additives on controlling the prolonged cycling performance of the high-voltage oxide cathode, focusing on examining their influence on the CEI. Ultimately, we examined the collective effect of enhanced interfaces on the overall cycling performance of the sodium ion full cell. An innovative approach to regulating the inner solvation structure of the carbonate electrolyte has been achieved by the inclusion of dual anion additives (tetrafluoroborate (BF_4^-) and (bis(trifluoromethane)sulfonimide (TFSI^-))) into the conventional carbonate electrolyte system, consisting of 1 M sodium hexafluorophosphate (NaPF_6) mixed in a 1:1 volumetric ratio of ethylene carbonate (EC) and propylene carbonate (PC). We found an enhanced ICE of the HC anode (39% to 78%) while promoting the formation of inorganic-rich SEI and CEI on the surfaces of the HC anode and high voltage $\text{Na}_{0.67}\text{Ni}_{0.33}\text{Mn}_{0.67}\text{O}_2$ (NMNO) oxide-based cathode, respectively. The participation of dual anion additives in the inner solvation shell around the Na^+ cation induces a change in reductive stability by raising the Lowest Unoccupied Molecular Orbital (LUMO) level of pure solvents and Na^+ -solvent complex as compared to the Na^+ -solvent-anion complex, as con-

firmed by the Density Functional Theory (DFT) calculations. The improved oxidative stability was also governed by lowering the HOMO energy level on the introduction of BF_4^- anion and the preferential participation of Na^+ -ECPC-TFSI⁻ complex formed an inorganic rich (sulfur and nitrogen containing) CEI that suppressed the unwanted side reactions on employing high voltage cathode. The preferential participation, along with the reduction and oxidation of dual anions, suppresses the decomposition of solvents on the surface of the Char1100 HC anode and NMNO cathode, yielding inorganic component-rich (F, S, N, and B) SEI and CEI, respectively confirmed through X-ray Photoelectron Spectroscopy (XPS) and High-Resolution Transition Electron Microscopy (HR-TEM). To gain deeper insights into the precise composition of the SEI on the HC surface, we employed a powerful and highly recommended Time of Flight Secondary Ion Mass Spectroscopy (TOF-SIMS) technique which confirmed the presence of inorganic fragments resulting from anion decomposition as these anions are located near Na^+ cation, as corroborated by Molecular Dynamics (MD) simulations. The inorganic-rich SEI formed on the HC anode not only formed thinner SEI to enhance ICE but also demonstrated improved rate capability attributed to enhanced diffusion kinetics, as validated by the Randles Sevcik's equation, Distribution of Relaxation Time (DRT) and desolvation energy calculations using Free Energy Perturbation (FEP) methods. The inorganic-rich CEI on the surface of the sodium metal nickel manganese oxide (NMNO) cathode was observed to mitigate transition metal dissolution confirmed through Inductive Coupled Plasma-Atomic Emission Spectroscopy (ICP-AES) and reduced structural degradations, contributing to enhanced long-term cycling performance in sodium-ion batteries.

Subsequently, a single-layer pouch cell incorporating the Char1100 HC anode and NMNO cathode in a dual anion additive added electrolyte was fabricated. This cell exhibited an initial cycle Coulombic efficiency of $\approx 79\%$, and it demonstrated the ability to deliver an areal capacity of 1.5 mA h cm^{-2} at a current rate of 0.25 mA cm^{-2} , retaining 82.6% of its initial discharge capacity even after 200 cycles.

2. Results and Discussion

2.1. Electrochemical Performance of Char1100 HC Half-Cell in Conventional (Conv) and Dual Salt Added (DS) Electrolyte

Char1100 HC anode was synthesized according to the procedure outlined in Schematic S1 (Supporting Information and characterized as depicted in Figure S1A–G (Supporting Information). Further details on characterization can be found in the supporting information file. The conventional electrolyte system is 1 M NaPF_6 EC:PC denoted as "Conv" and the dual-salt added electrolyte system is 1 M NaPF_6 EC:PC + 0.1 M NaTFSI + 0.1 M NaBF_4 EC:PC denoted as "DS" throughout the manuscript. The electrochemical performance of the Char1100 HC anode in Conv and DS electrolytes was investigated to show the effect of anion additives. The cyclic voltammogram profile of the Char1100 HC anode in the Conv electrolyte (Figure 1A) shows 2 major peaks ≈ 1 and 0.38 V versus Na/Na^+ in the first cycle, corresponding to the formation of SEI on the surface of HC. The peak at 1 and 0.38 V is attributed to the reduction of solvent molecules to form SEI^[26] and the irreversible trapping of Na^+ ions into the

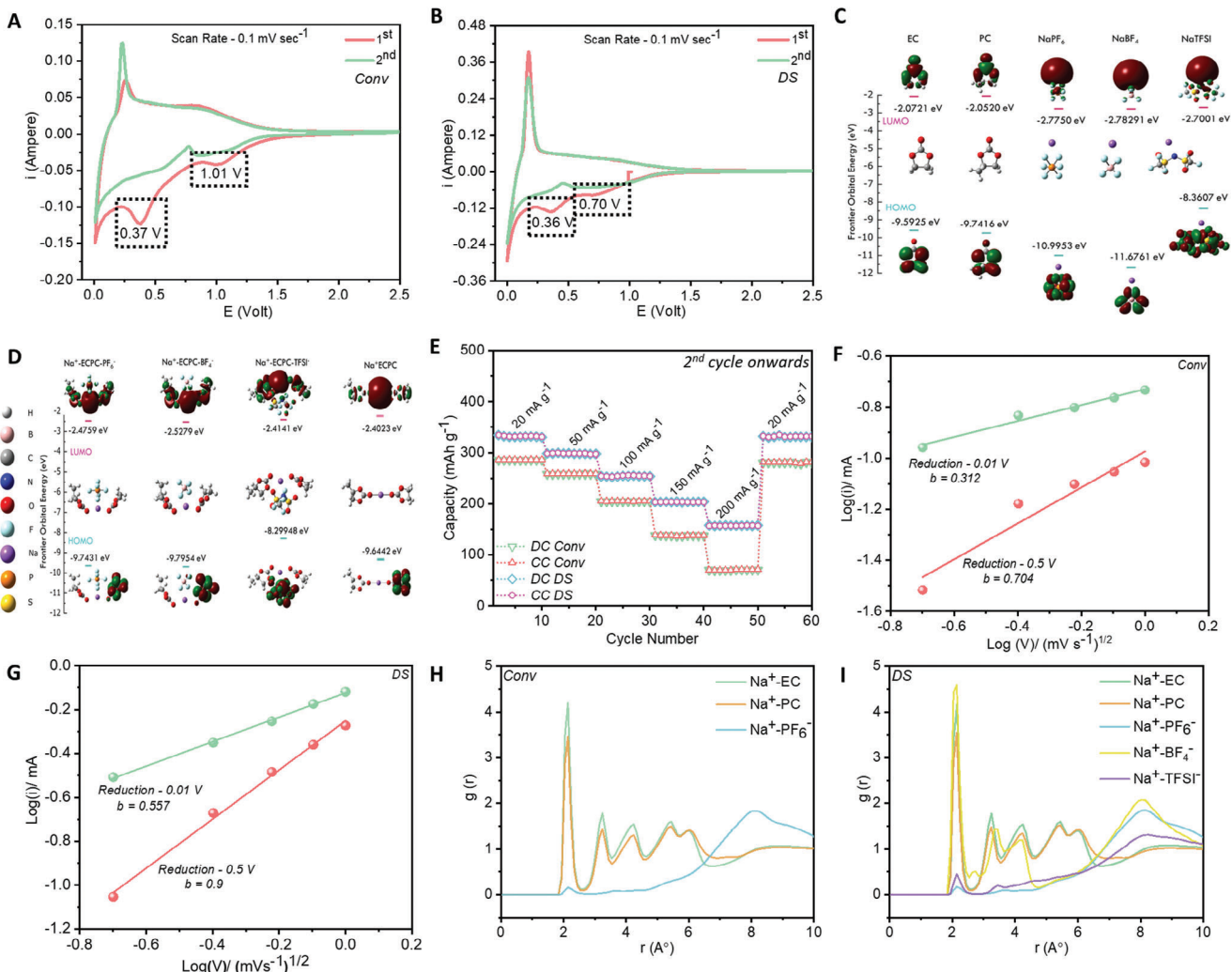


Figure 1. Cyclic voltammogram profile of Char1100 HC anode in A) Conv and B) DS electrolyte at a scan rate of 0.1 mV sec^{-1} ; C) HOMO-LUMO energy levels for individual solvent and salt molecules of Conv and DS electrolyte; D) HOMO-LUMO energy levels for Na^+ -solvent anion complexes and Na^+ -solvent complex; E) Rate capability test for Char1100 HC anode at different current rates in Conv and DS electrolyte; Linear fitting for calculating the value of b from Randles Sevcik's equation in F) Conv and G) DS electrolyte; Radial distribution function to check the solvation structure around Na^+ cation for H) Conv and I) DS electrolyte.

defective sites on the surface of HC,^[27] respectively. The CV profile of the Char1100 HC anode showed a shift in the position of the peaks to lower voltages ($1\text{--}0.7 \text{ V}$ and $0.38\text{--}0.36 \text{ V}$) in the case of DS electrolyte (Figure 1B), confirming the change in the reduction pathways on the surface of HC on the addition of dual anion additives. The shift in peak from 1 to 0.7 V is likely indicative of the enhanced reductive stability of solvent molecules, attributed to the introduction of highly coordinating BF₄⁻ and TFSI⁻ anions in the inner-solvation shell of Na-ion in DS electrolyte. This phenomenon is expected to reduce the overall extent of solvent reduction on the surface of the Char1100 HC anode material,^[25] thereby homogeneously distributing SEI components on the surface of the anode to form a thin and robust SEI. This has been substantiated by comparing the LUMO levels between pure solvent molecules, Na⁺-solvent, and the Na⁺-solvent-anion complexes. The analysis revealed decreased LUMO energy levels upon introducing anions into the electrolyte system compared to

the pure solvent molecules and Na⁺ cation coordinated solvent complex (Na⁺-ECPC), as shown in Tables S1 and S2 (Supporting Information). The findings indicate that the Na⁺-ECPC-anion complexes are likely to act as the primary interphase precursors, undergoing electrochemical reduction at the HC surface prior to Na⁺-ECPC. This process results in an SEI with a prominent chemical fingerprint derived from these anion complexes.^[28]

In a mixture of salts and solvents, the anions associated with different Na-based salts can strongly influence the chemical stability of electrolytes in primarily 2 ways: i) the Highest Occupied Molecular Orbital (HOMO) level of anions limits the oxidative stability of electrolyte and ii) the LUMO level of anions facilitate the formation of SEI.^[20] Herein, we have investigated the SEI formation in the electrolyte containing the combination of different Na-based salts and solvents; thus, the LUMO level of all the component salts and solvents has been calculated. Figure 1C depicts the frontier orbitals (HOMO and LUMO) of salts –NaPF₆,

NaBF_4 , and NaTFSI , along with the solvent molecules –EC and PC. The LUMO energy level distinctly shows a declination in values from the solvents to salts, which follows the sequence $\text{NaBF}_4 < \text{NaPF}_6 < \text{NaTFSI} < \text{EC} < \text{PC}$. The lowest LUMO value indicates a preferential reduction of that specific component in the electrolyte. In this case, NaBF_4 has the lowest LUMO value among the other components, approximating its active participation in the SEI layer formation. These observations correspond well with the MD simulation (*discussed later*), and the ex-situ XPS analysis, where the radial distribution function estimates the coordination number of BF_4^- in the first solvation shell is higher than the other constituent anions. To account for the role of cation-solvent-anion coordination in SEI formation, we have additionally optimized the LUMO level of each salt in the presence of both solvents, EC and PC. One EC and one PC molecule have been considered with each salt for simplicity. We have assumed an equal contribution from EC and PC, considering that the coordination number of both solvent molecules is nearly identical in the electrolytes (Table S3, Supporting Information). On introducing anion in the solvents, the LUMO energy levels for the Na^+ -solvent-anion (Figure 1D) complex shift to lower values as compared to pure solvent molecules from $-2.0\ 7215\ \text{eV}$ for EC and $-2.0\ 5201\ \text{eV}$ for PC to $-2.4759\ \text{eV}$ for $\text{Na}^+\text{-ECPC-PF}_6^-$, $-2.5279\ \text{eV}$ for $\text{Na}^+\text{-ECPC-BF}_4^-$ and $-2.4141\ \text{eV}$ for $\text{Na}^+\text{-ECPC-TFSI}^-$ respectively. The LUMO level of the $\text{Na}^+\text{-ECPC}$ complex was also found to be higher ($-2.4023\ \text{eV}$) than the LUMO energy levels of all $\text{Na}^+\text{-ECPC}$ -anion complexes. This indicates that the Na^+ cation is withdrawing fewer electrons from the solvent molecules (either pure or coordinated) when anions are introduced into the electrolyte system, thereby improving the reductive stability of the Na^+ -solvent complex. These anions can form strong bonds with the Na^+ cation, supplying electrons to the cation for the reduction reactions taking place on the HC anode surface. Interestingly, on the introduction of anions, the previous sequence of LUMO energy levels, as followed by individual anions in the electrolyte, still persists, i.e., NaBF_4 coordinated with EC and PC ($\text{Na}^+\text{-ECPC-BF}_4^-$) tends to reduce first and contribute to SEI formation earlier than other Na^+ -solvent-anion complexes. The sequence also predicts the compositions of the multilayer SEI; the inner layer of SEI adjacent to HC primarily consists of inorganic decomposition products arising from anions, which is covered by the outer organic layer of SEI consisting of decomposition products from the solvent molecules. The estimated HOMO-LUMO values for each structure are tabulated in Tables S1 and S2 (Supporting Information).

Similarly, on introducing anions in the pure solvents, the HOMO energy levels of Na^+ -solvent-anion complex shift toward lower values from $-9.59\ 256\ \text{eV}$ for EC and $-9.74\ 168\ \text{eV}$ for PC to $-9.7431\ \text{eV}$ for $\text{Na}^+\text{-ECPC-PF}_6^-$ and $-9.7954\ \text{eV}$ for $\text{Na}^+\text{-ECPC-BF}_4^-$ respectively except for $\text{Na}^+\text{-ECPC-TFSI}^- (-8.2994\ \text{eV})$ where a shift toward higher value was found. The decrease in the HOMO levels when 2 salt anions (PF_6^- and BF_4^-) are present in the system is indicative of the improved oxidative stability of the electrolyte. However, the increase in HOMO level on the introduction of TFSI^- anion will cause preferential decomposition of the $\text{Na}^+\text{-ECPC-TFSI}^-$ complex. This will yield CEI rich in S and N containing inorganic components that may further reduce the unwanted side reactions between the cathode and the electrolyte on prolonged cycling. When present in the CEI, these compo-

nents also help reduce the transition metal dissolution, as proved through XPS and ICP-AES analysis in the later section of the discussion. The role of NaTFSI salt in reducing vanadium dissolution in sodium vanadium fluorophosphate cathode (NVPF) has already been reported earlier.^[29]

Figure S2A,B (Supporting Information) shows the voltage versus capacity (charge-discharge) profile of the Char1100 HC anode in the Conv electrolyte and DS electrolyte at a current rate of $50\ \text{mA g}^{-1}$, respectively. The first discharge/charge capacity values for Char1100 HC anode in Conv and DS electrolytes are $641.23/256.61\ \text{mAh g}^{-1}$ and $403.16/309.90\ \text{mAh g}^{-1}$, respectively. The second discharge/charge capacity values for Char1100 HC anode in Conv and DS electrolytes are $249.65/246.73$ and $312.89/303.91\ \text{mAh g}^{-1}$, respectively. The higher second discharge capacity in the DS electrolyte indicates more effective use of reversible sodium storage sites, which are otherwise obstructed by the formation of a thicker SEI and other side reactions in the case of the Conv electrolyte.^[30] The ICE of the HC anode was found to be 39% and 78% in Conv and DS electrolytes, respectively, reflecting the enhanced ICE in the DS electrolyte. This improvement is attributed to the formation of a thinner SEI with higher inorganic content, enriched with elements like fluorine (F), boron (B), sulfur (S), and nitrogen (N) from the reduction of dual salt additive anions as discussed previously. In contrast, as there is a major participation of solvent species around Na^+ in the primary solvation shell in the case of Conv electrolyte, the solvent species dominantly engage in the initial reduction process to form SEI rich in organic components. We also examined molar ratios of 0.05:0.05, 0.1:0.1, 0.15:0.15, and 0.2:0.2 to evaluate the impact of anion additive concentration on HC electrode performance. Detailed charge-discharge profiles of the HC anode under these ratios are presented in Figure S3A–D (Supporting Information). Our investigations revealed a reduction in electrolyte ionic conductivity with increasing salt anion additive concentration, from $8.641\ \text{mS cm}^{-1}$ for 0.05:0.05 to $7.962\ \text{mS cm}^{-1}$ for 0.2:0.2 molar ratio of additives. While there was a marginal enhancement in the ICE of HC, from 78% to 81.4%, the resultant decline in electrolyte ionic conductivity notably elevated the total impedance of the cell, as depicted in Figure S3E–H. This phenomenon can adversely affect the long-term cycling performance of the HC anode.

We further found that the formation of thinner and better interphase on the Char1100 HC anode in the DS electrolyte subsequently leads to a better rate capability (Figure 1E), providing a capacity of $157\ \text{mAh g}^{-1}$ at a current rate of $0.2\ \text{A g}^{-1}$ as compared to a capacity of only $69\ \text{mAh g}^{-1}$ in the case of Conv electrolyte respectively. While there was a minor decline in the charge-discharge capacity of the Char1100 HC anode when transitioning from 20 to $50\ \text{mA g}^{-1}$ in the Conv electrolyte compared to the DS electrolyte, a significant decrease occurred at higher current rates (150 and $200\ \text{mA g}^{-1}$) in the Conv electrolyte. This indicates that the diffusion of Na^+ ions through the SEI is slower for the Char1100 HC anode due to the formation of a thicker SEI in the Conv electrolyte. The average discharge capacity for Conv electrolyte was $286.30\ \text{mAh g}^{-1}$ ($\text{SD} = 0.6$), $258.48\ \text{mAh g}^{-1}$ ($\text{SD} = 0.69$), $205.1\ \text{mAh g}^{-1}$ ($\text{SD} = 0.43$), $138.66\ \text{mAh g}^{-1}$ ($\text{SD} = 0.12$), and $70.28\ \text{mAh g}^{-1}$ ($\text{SD} = 0.21$) at a current rate of 20, 50, 100, 150, and $200\ \text{mA g}^{-1}$. The average discharge capacity for DS electrolyte was $334.66\ \text{mAh g}^{-1}$ ($\text{SD} = 0.02$), $298.32\ \text{mAh g}^{-1}$

(SD – 0.05), 254.3 Ah g⁻¹ (SD – 0.14), 203.03 mAh g⁻¹ (SD – 0.05), and 156.55 mAh g⁻¹ (SD – 0.04) at a current rate of 20, 50, 100, 150, and 200 mA g⁻¹. The improved rate capability was further confirmed by the higher value of b in DS electrolyte obtained from linear fitting through Randles Sevcik's equation, as shown in Figure 1F,G. The details of the calculation are provided in (Figure S4, Supporting Information). A higher b value for either peak at a low voltage plateau (0.01 V) or a sloping voltage (0.5 V) for the DS electrolyte signifies a surface-controlled reaction within the DS electrolyte, contributing to enhanced kinetics for the HC anode. In contrast, a lower "b" value (0.31 for the peak at 0.01 V and 0.70 for the peak at 0.5 V) in the Conv electrolyte, as shown in Figure 1F,G, suggests a less favorable kinetics for the Char1100 HC anode. Based on the results above, we can infer that the Char1100 HC anode, cycled in the DS electrolyte, exhibits enhanced ICE, greater reversibility, and improved rate capability compared to a conventional electrolyte. MD simulations were conducted to explore further the influence of solvation structure on the degradation of electrolyte components at the anode's surface and to understand the underlying reasons for the improved electrochemical performance.

2.2. Investigation of the Solvation Structure through Molecular Dynamics (MD) Simulations and Spectroscopy

The solvation structure of electrolytes is usually examined through a combination of experimental and computational techniques.^[31–38] We have also employed MD simulations along with Raman and Fourier Transform Infrared (FTIR) spectroscopies to investigate the solvation structure around Na⁺ cation in Conv and DS electrolytes. The solvation structure around the Na⁺ cation was investigated through MD simulations after equilibration under constant NPT conditions. The final snapshots of the solvation structure around Na⁺ cation within a radius of 5 Å obtained through MD simulations in Conv and DS electrolyte are shown in Figure S5A,B (Supporting Information). Analysis of the radial distribution function (RDF) reveals that EC and PC exhibit reduced coordination numbers in DS electrolytes compared to Conv electrolytes, as illustrated in Figure 1H,I, respectively. Moreover, the PF₆⁻ anion exhibits a low coordination number of 0.005 in the Conv electrolyte but a slightly higher value of 0.015 in the DS electrolyte, indicating enhanced primary anion participation in introducing additives. Like the primary salt anion (PF₆⁻), the dual salt additive anions (BF₄⁻ and TFSI⁻) were also found to participate in the primary solvation shell in DS electrolyte, showing RDF values of 2.10 and 2.14 Å, respectively. The predominant involvement of the BF₄⁻ anion in the primary solvation shell, revealed by its highest coordination number of 0.026 among all the anions, fosters a robust interaction between Na⁺ and BF₄⁻, culminating in the generation of Na_xBF_yO_z and NaF.^[39] The coordination number of each salt, solvent, and additive molecule for Conv and DS electrolyte is shown in Table S3 (Supporting Information), indicating the highest participation of BF₄⁻ anion after EC and PC in the DS electrolyte, whereas the preferential involvement of only solvent molecules in the case of Conv electrolyte. Further, the detection of Na–F and B–F bonds in XPS spectra confirms the role of BF₄⁻ anion in forming SEI, as discussed in the subsequent section. Therefore, the final solva-

tion structure around Na⁺ cation for Conv and DS electrolyte can be shown through the Schematic shown in Schematic S2 (Supporting Information).

Further, the involvement of dual anion additives can be ascribed to the higher donor number of BF₄⁻ and TFSI⁻ anions in comparison to PF₆⁻ anion.^[40] This characteristic assists in disrupting the robust interaction between the solvent and Na⁺ cation, as can be confirmed through reduced solvent coordination number in DS electrolyte, consequently mitigating solvent reduction during the initial galvanostatic discharge. The involvement of dual anions in the primary solvation shell induces the formation of inorganic components-rich interphases on both the anode and cathode, ensuring the establishment of stable interphases for prolonged cycling stability in both half cells and full cells when employing the DS electrolyte system.

The Raman peak at a wavelength of 715 and 722 cm⁻¹ corresponds to the free EC molecules,^[41,42] and EC coordinated to Na⁺ cation does not change much on the addition of dual anion additives in DS electrolyte. However, a sharp narrowing of peak shape (Figure S6A,B, Supporting Information) can be observed when adding dual anion additives in the electrolyte, indicating a decrease in interaction between Na⁺ and EC.^[43] A peak at 740 cm⁻¹ was observed, indicating the presence of free PF₆⁻ molecules in the Conv electrolyte. In the case of DS electrolyte, the peak corresponds to a combination of free PF₆⁻ and TFSI⁻ anions.^[42] The peak intensity for the coordination of Na⁺ and PF₆⁻ or TFSI⁻ anions at \approx 744 cm⁻¹^[44] increases on adding dual anion additives in the electrolyte indicative of the increased anion participation in DS electrolyte.

Figure S7A (Supporting Information) shows the comparison of FTIR spectra of the mixture of EC:PC (denoted as EC:PC in Figure–green), EC:PC + NaTFSI (denoted as TFSI⁻ in Figure – blue), and EC:PC + NaBF₄ (denoted as BF₄⁻ in Figure–Pink). Apart from the peaks that are present in the FTIR spectra of EC:PC mixture, TFSI⁻ and BF₄⁻ spectra consist of some extra peaks that are being denoted to free BF₄⁻ at 528.1 cm⁻¹,^[45] free TFSI⁻ at 513.9 and 613.4 cm⁻¹,^[46] Na⁺ coordinated to BF₄⁻ at 1698.6 cm⁻¹ and Na⁺ coordinated to TFSI⁻ at 1347.5 cm⁻¹ respectively. Figure S7B (Supporting Information) shows the comparison of FTIR spectra of the mixture of EC:PC (denoted as EC:PC in Figure – green), DS (black), and Conv (red) electrolytes. The presence of the free BF₄⁻ (515.8 cm⁻¹), TFSI⁻ (620.7 cm⁻¹), PF₆⁻ (1014.2 and 1282.3 cm⁻¹)^[46] and their coordination with Na⁺ cation (Na⁺-BF₄⁻ at 1357.5 cm⁻¹ and Na⁺-TFSI⁻ at 1692.7 cm⁻¹) were assigned taking the reference of the FTIR spectra where single anions were being mixed with EC and PC.

From Raman and FTIR spectra, we can conclude that on adding dual salt additives in the Conv electrode, both BF₄⁻ and TFSI⁻ anions are participating in the solvation around Na⁺ along with the solvation from PF₆⁻ supporting our MD simulation results.

2.3. Study on the Composition and Microstructure of SEI

The microstructure and chemical composition of SEI formed on the surface of the Char1100 HC electrode recovered after a hundred charge-discharge cycles in Conv and DS electrolyte was investigated through XPS and HR-TEM combined with High

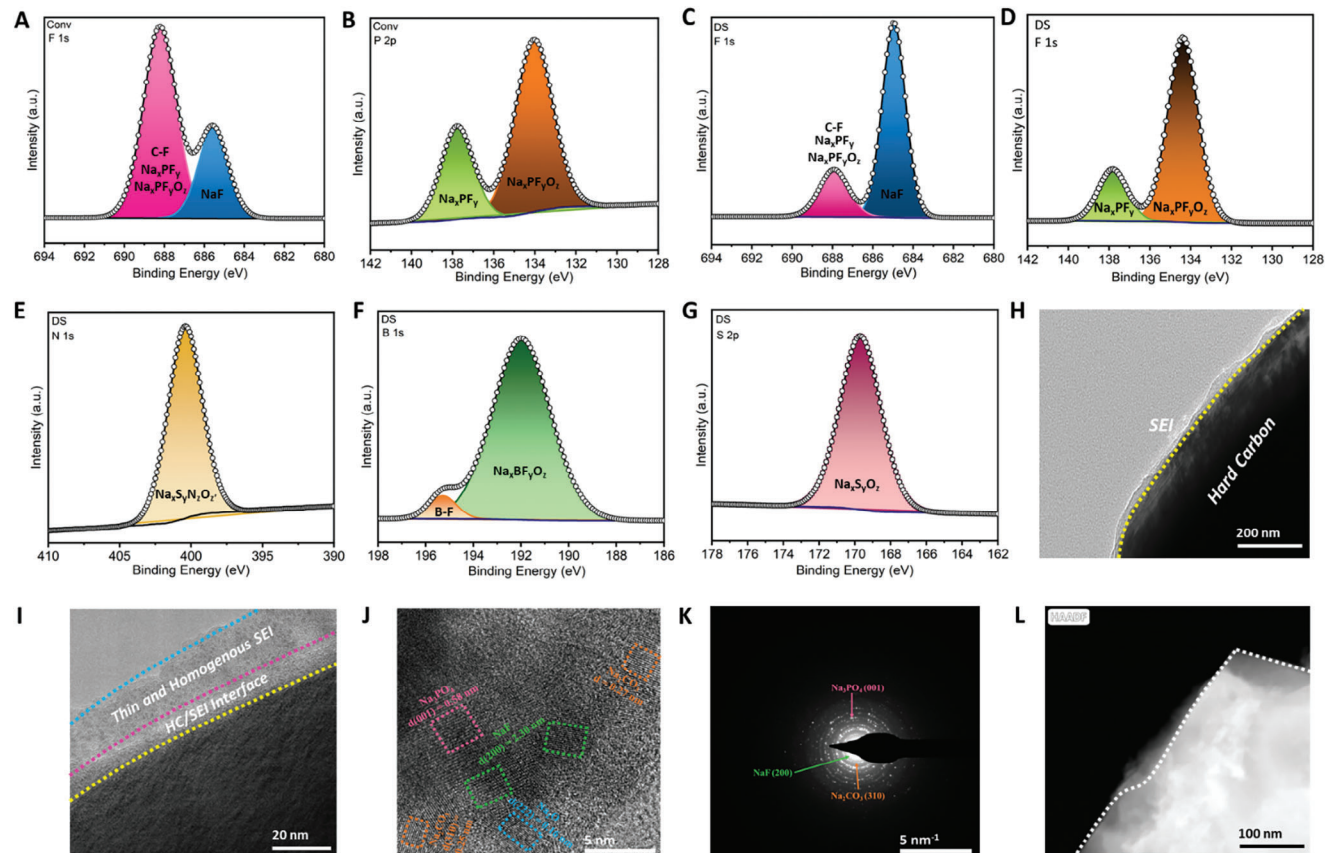


Figure 2. Chemical composition of SEI formed on the surface of Char1100 HC through A) F 1s and B) P 2p XPS for Conv electrolyte; C) F 1s, D) P 2p, E) N 1s, F) B 1s and G) S 2p XPS for DS electrolyte; Structure of SEI formed on the surface of HC through H), and I) TEM image showing the formation of a uniform and stable SEI on the surface of Char1100 HC after 100 cycles; J) HRTEM image showing the presence of inorganic crystallites in SEI; K) SAED pattern and L) HAADF-STEM image taken on the surface of HC cycled in DS electrolyte.

Angle Annular Dark-Field Scanning TEM (HAADF-STEM) imaging. For compositional analysis, F 1s XPS spectra of HC electrode cycled in Conv electrolyte (Figure 2A) show 2 peaks at 688.2 and 685.5 eV, corresponding to the formation of Na_xPF_y/Na_xPF_yO_z^[47] and NaF,^[15] respectively. Similar components of SEI are confirmed through the P 2p XPS, showing peaks at 137.7 eV for Na_xPF_y^[48] and 134.03 eV for Na_xPF_yO_z,^[49] respectively, as shown in Figure 2B. It is interesting to note that the ratio of NaF to Na_xPF_y/Na_xPF_yO_z in the case of Conv electrolyte is much lesser as compared to the DS electrolyte, where the amount of NaF in the SEI composition is much higher because of the decomposition of the combination of dual additive anions (BF₄⁻ and TFSI⁻) as shown in Figure 2C,D respectively. Figure S8B,E (Supporting Information) show the C 1s XPS spectra of the HC electrode in Conv and DS electrolytes, respectively. The preferential reduction of EC and PC solvents in Conv electrolyte leads to many organic components such as carbonates, sodium alkoxides, and sodium alkyl carbonates.^[50] In contrast, the preferential reduction of dual additive anions in the case of DS electrolyte leads to the formation of inorganic components such as NaF (685 eV),^[15] Na_xPF_yO_z (134.6 eV),^[49] Na_xBF_yO_z (192.02 eV),^[51] Na_xS_yO_z (169.7 eV),^[48] and Na_xS_yN_zO_z (400.4 eV).^[48] The presence of nitrogen, boron, and sulfur inorganic components in addition to fluorine and phosphorous compounds in the SEI is fur-

ther confirmed through N 1s, B 1s, and S 2p XPS of the HC electrode as shown in Figure 2E–G, respectively. The estimated reduction pathways for forming these organic and inorganic components are mentioned in Equations S1–S9 (Supporting Information).

The presence of N, B, and S containing inorganic components has already been found to be advantageous to the SEI reported in the literature. The boron-containing species (B–O and B–F) with high ionic conductivity are seen as effective in serving as a SEI binder. This function involves tightly bonding both the inorganic components and the organic polymer, ultimately contributing to forming a resilient and flexible SEI layer.^[52]

Additionally, the presence of sulfur and nitrogen-containing species in the SEI is found to possess a lower diffusion energy barrier of Na⁺, reduce the interfacial resistance, and boost Na migration kinetics, thereby improving the Na⁺ diffusion kinetics of the Char1100 HC anode.^[53]

To investigate the structure of SEI formed on the surface of the HC anode in Conv and DS electrolytes further, HR-TEM imaging was done along with HAADF-STEM imaging. Figure 2H shows the TEM imaging of an HC particle with a uniform SEI coated on its surface when cycled in DS electrolyte for prolonged cycling (100 cycles). On magnification, a thin and homogenous SEI of thickness ≈20–25 nm was found, as shown in Figure 2I, in

contrast to the thickness of more than 50 nm in the case of Conv electrolyte (Figure S8, Supporting Information). The HR-TEM imaging of SEI (Figure 2I) shows the presence of lattice fringes from some inorganic crystallites. The d-spacing calculated from the lattice fringes obtained from HR-TEM (Figure 2J) matches with the d-spacing of Na_3PO_4 ($d = 0.58 \text{ nm}$), Na_2O ($d = 0.16 \text{ nm}$), Na_2CO_3 ($d = 0.27 \text{ nm}$), and NaF ($d = 2.30 \text{ nm}$).^[6,54] Similar components were indexed in the diffraction pattern taken over the SEI on the surface of the Char1100 HC anode, as shown in Figure 2K. Unfortunately, the lattice fringes from the decomposition product from NaTFSI salt could not be identified through HR-TEM imaging. However, such components could potentially be identified with greater clarity and precision using high-resolution and aberration correction TEM instruments, which, unfortunately, were not accessible for our study. Figure 2L shows the HAADF-STEM image of SEI formed on the surface of the Char1100 HC anode in the DS electrolyte. In summary, a thin, homogenous, and inorganic component-rich robust SEI was found on the surface of the Char1100 HC anode because of the preferential reduction of dual salt additives in the DS electrolyte confirmed through XPS and HR-TEM techniques.

On the contrary, SEI on the surface of the Char1100 HC anode was observed to be thicker and non-uniform in the Conv electrolyte. Figure S9A,B (Supporting Information) display TEM images of the SEI formed on the Char1100 HC anode in the Conv electrolyte, revealing an average thickness exceeding 70 nm. The generation of a thicker, non-uniform, and porous SEI was additionally validated through the HAADF-STEM image (Figure S9C, Supporting Information). Individual color-coded EDS maps for Na (red), C (green), O (blue), F (purple), and P (pink) are depicted in Figure S9D–H (Supporting Information). The mixed color map for the SEI (Figure S9I, Supporting Information) further verifies the prevalence of predominantly organic components on the Char1100 HC anode surface in the Conv electrolyte.

To further confirm the role of dual anion additives, we precisely investigated the composition of SEI formed on the surface of HC employing a powerful TOF-SIMS technique for HC cycled in Conv and DS electrolyte after 10 cycles. We consider 10 charge-discharge cycles to ensure the completion of the reduction or interfacial modification process occurring on the surface of HC during the initial cycles, facilitating the formation of a complete SEI. Figure 3A–D and Figure 3E–H show the TOF-SIMS spectra in positive secondary ion mode collected from the surface of Char1100 HC anode cycled in Conv and DS electrolyte for 10 cycles respectively. The intensity ratio of $\text{Na}_2\text{F}^+/\text{Na}_2\text{OH}^+$ coming from the decomposition of salt anions is clearly more for the DS electrolyte, as shown in Figure 3C. This suggests an increased decomposition of anions during the SEI formation due to the close involvement of anions around the Na^+ cation, as demonstrated by our MD simulation findings. Along with the formation of NaF , we found the presence of decomposition products from NaBF_4 and NaTFSI additives at $m/z = 72$ from Na_2BO_2^+ (Figure 3G) and $m/z = 117 \text{C}_7\text{H}_5\text{N}^+$ (Figure 3H) respectively, in the mass spectra of HC cycled in DS electrolyte whereas these peaks were completely absent in the mass spectra of HC cycled in Conv electrolyte (Figure 3C,D). Figure 3I–K and Figure 3L–N show the TOF-SIMS spectra in negative secondary ion mode collected from the surface of Char1100 HC anode cycled in Conv and DS electrolyte for 10 cycles respectively. The presence of the decomposition prod-

ucts from dual salt anions was also evident at $m/z = 32$ from S^- , $m/z = 37$ from NaN^- , $m/z = 48$ from SO^- , and $m/z = 49$ from BF_2^- as shown in Figure 3M which were absent in the mass spectra of HC cycled in Conv electrolyte. All the nitrogen-containing ($\text{C}_7\text{H}_5\text{N}^+$ and NaN^-), sulfur-containing (S^- and SO^-), and boron-containing (Na_2BO_2^+ and BF_2^-) decomposition products are marked with red, green, and blue stars in Figure 3, respectively. Apart from the assigned m/z peaks, we found various unknown peaks (marked as black stars) clearly revealing the distinct nature of SEI formed in Conv and DS electrolyte. Therefore, we can summarise that the presence of these inorganic fragments coming from the decomposition of dual anions identified in the TOF-SIMS mass spectra strongly supports our hypothesis regarding the modification of the solvation structure around the Na^+ cation upon adding dual anion additives. The highlights of investigated features of SEI on the surface of HC from the TOF-SIMS analysis are displayed in the box in Figure 3O for Conv and DS electrolytes, respectively.

In summary, incorporating dual anion additives has facilitated forming and preserving a thin, homogeneous, and inorganic-rich SEI layer even after prolonged cycling. Consequently, these improvements have enhanced coulombic efficiency, kinetics, cycling stability, and reduced impedance for charge-transfer processes on the HC anode.

2.4. Transport Properties of Na^+ Cation in Conv and DS Electrolyte

The transport of Na^+ ions within the bulk electrolyte is a critical factor influencing the battery's performance and safety of the battery.^[55] Key battery parameters like capacity, cycling stability, and rate capability are intricately linked to the transport properties of the electrolyte, encompassing factors such as ionic conductivity, ionic mobility, transference number, and the diffusion of Na^+ ions within the bulk electrolyte. In this section, we will explore the correlation between the transport properties of Conv and DS electrolytes and the electrochemical performance of the Char1100 HC anode against sodium.

The ionic conductivity of Conv and DS electrolytes were measured to be 8.893^1 and 8.293 mS cm^{-1} , respectively. The slight decline in ionic conductivity upon introducing dual anion additives can be attributed to the formation of a bulkier and loose solvation structure defined by a lower total coordination number (5.57) around Na^+ as compared to Conv electrolyte (6.005), characterized by the predominant involvement of the BF_4^- anion in the primary solvation shell. The difference in ionic conductivity values in Conv and DS electrolytes is supported by the Mean Square Displacement (MSD) and self-diffusion coefficients ($0.057 \text{ \AA}^2 \text{ ns}^{-1}$ for Conv and $0.050 \text{ \AA}^2 \text{ ns}^{-1}$ for DS) calculated through MD simulations as shown in Figure 4A.

The transference number of Na^+ cation was significantly higher for DS ($t_{\text{Na}^+} = 0.54$) compared to the Conv electrolyte ($t_{\text{Na}^+} = 0.36$), as shown in Figure 4C,B respectively. A high transference number in the DS electrolyte can alleviate concentration polarisation during charge-discharge cycles, leading to increased rate capability,^[56] as is evident in the electrochemical performance of the Char1100 HC anode cycled in the DS electrolyte at different current rates (Figure 1E).

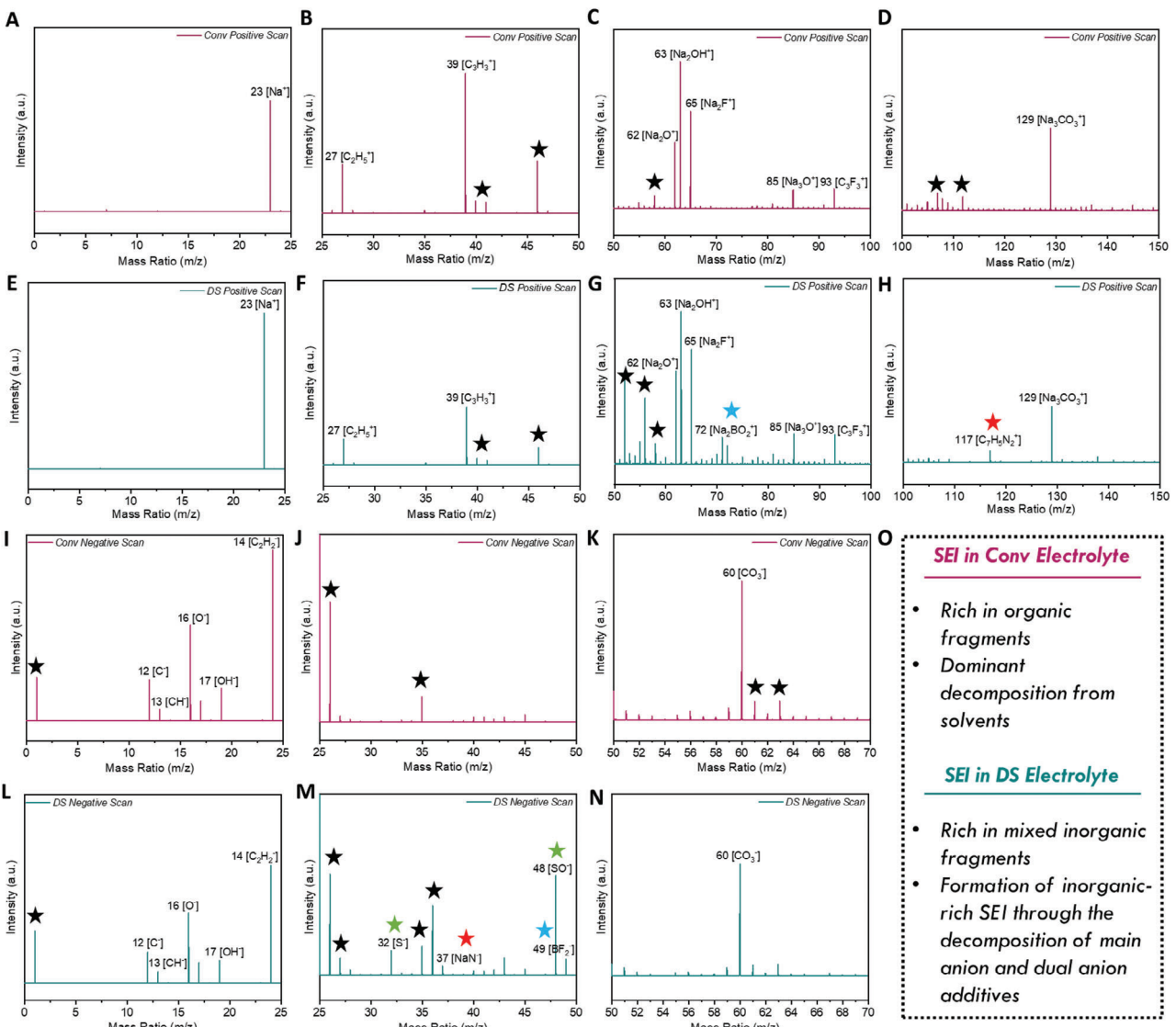


Figure 3. TOF-SIMS spectra of positive secondary ion mode for Char1100 HC after 10 cycles in A–D) Conv electrolyte and E–H) DS electrolyte; TOF-SIMS spectra of negative secondary ion mode for Char1100 HC after 10 cycles in I–K) Conv electrolyte and L–N) DS electrolyte; O) Characteristic of SEI formed on the surface of HC in Conv and DS electrolyte.

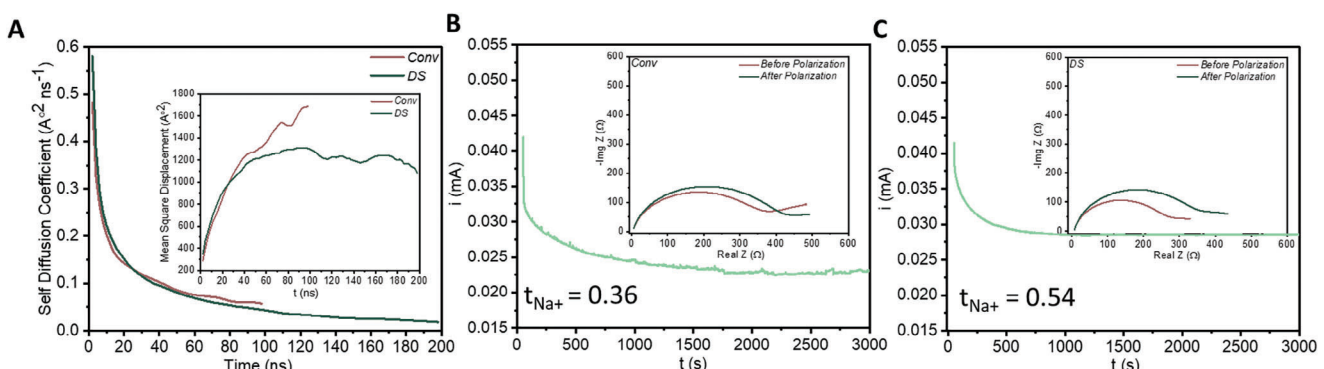


Figure 4. A) Self-diffusion coefficient for bulk Conv and DS electrolyte (inset showing the mean square displacement for Conv and DS electrolyte); Transference number calculation for B) Conv and C) DS electrolyte (insets showing Nyquist impedance plots for Na/Na symmetric cells before and after polarization).

The primary cause of impedance in batteries often arises from the mobility of cations within the bulk electrolyte. The selection of anions significantly influences mobility. The cation mobility is derived from the product of conductivity and the cation transference number, which is higher in the DS electrolyte than the Conv electrolyte, indicating lower impedance processes in the DS system, discussed in more detail in the next section. To further explore the mobility of Na^+ ions in the 2 electrolyte systems, we conducted FEP calculations. FEP simulations enable the direct numerical assessment of the free energy of solvation of ions in the electrolytes, offering a deeper understanding of the impact of dual anion additive on Na^+ ion diffusion in the liquid electrolyte. The charging free energies for a Na^+ ion in the liquid electrolytes are $-119.0 \pm 0.13 \text{ kcal mol}^{-1}$ for the Conv electrolyte and $-117.8 \pm 0.15 \text{ kcal mol}^{-1}$ for the DS electrolyte, respectively. More negative free energy indicates stronger ion-electrolyte interactions, resulting in increased resistance to Na^+ ion migration across the interphase and, consequently, slower ion diffusion. From the comparison of free energy analysis and the value of b from Randles Sevcik's equation, we may conclude that low (less negative) free energy, higher b value at enhanced scan rates, and good electrode-electrolyte interface are critical features of the DS electrolyte, offering enhanced rate performance in Char1100 HC anode. All the transport properties of Conv and DS electrolytes are listed in Table S4 (Supporting Information).

2.5. Distribution of Relaxation Time (DRT) of Char1100 HC in Conv and DS Electrolyte

The DRT method enables the differentiation of electrochemical processes with varying time constants derived from electrochemical impedance data. This approach provides a more distinct perspective on the measured spectra, aiding in resolving processes that might go unnoticed using other methods.

The analysis of the DRT was performed to separate the distinct contributions from various processes occurring during the 1st discharge and 1st charge in the Char1100 HC anode through time domain characteristics. Corresponding to the voltage points indicated in Figure S10A–D, we have taken Electrochemical Impedance Spectroscopy (EIS) during 1st discharge and 1st charge of the Char1100 HC anode in both Conv and DS electrolytes, respectively. On deconvolution of DRT, we found the presence of 4 distinct processes denoted as P1, P2, P3, and P4, as described in the Schematic shown in Figure 5A. We have indicated these processes as follows, taking reference from^[57]

- P1: Diffusive mass transfer of Na^+ ions through SEI on HC electrode.
- P2: Charge transfer process through HC electrode.
- P3: Electron transfer process in the defective carbon to reduce the preadsorbed Na^+ ions.
- P4: Electron transfer process to deposit Na metal into the HC pores.

In both electrolytes, process P1 dominates at higher voltages (1.1 and 0.3 V) during SEI formation but diminishes toward the end of discharge (0.01 V). Na^+ ion diffusion through SEI is faster in DS electrolytes, indicated by a shorter time constant ($\log(\tau)$) for P1 than in Conv electrolytes. Additionally, the impedance

to Na^+ ion diffusion through SEI is smaller in DS electrolytes (Figure 5G–K) compared to Conv electrolytes (Figure 5B–F), as indicated by the reduced $\gamma(\Omega)$. These findings align with our previous observations of accelerated kinetics for the diffusion of Na^+ ions through HC electrodes in DS electrolytes. The charge transfer process (P2) in the DS electrolyte occurs so rapidly that it cannot be discerned separately from process P1 in the DRT. Conversely, the DRT of the Conv electrolyte indicates a slower charge transfer process, as indicated by the increased $\log(\tau)$. Changing the electrolyte has minimal impact on the impedance of the pore-filling process of HC (P4), except for a slightly reduced impedance for pore filling in the case of DS electrolyte. This observation further aligns with our earlier findings of the sustained plateau capacity due to improved kinetics for pore filling on HC, even at higher current rates in DS electrolytes. However, during 1st charge (Figure S11A–J, Supporting Information), all the processes possess lower impedance in the DS electrolyte than in the Conv electrolyte. Additionally, the time constant ($\log(\tau)$) for diffusive mass transfer of Na^+ ions through SEI and charge transfer of Na^+ ions through the Char1100 HC electrode is found to be sluggish for Conv electrolyte as compared to DS electrolyte, which further confirms the role of electrolytes in modulating the various electrochemical processes especially the kinetics of the Char1100 HC anode.

2.6. Electrochemical Performance of NMNO Half-Cell in Conv and DS Electrolyte

Before exploring the full cell's electrochemical performance, we examined the electrochemical performance of a half-cell consisting of the high-voltage NMNO cathode against Na metal and optimized the long cycling performance of NMNO half-cells taking different molar ratios of dual anion additives as shown in Figure S12A–D (Supporting Information). As illustrated in Figure S16A–D, there is a notable reduction in capacity loss (24.1%–15.1%) after 200 cycles as the molar ratios transition from 0.05:0.05 to 0.1:0.1. However, the capacity loss for molar ratios of 0.1:0.1, 0.15:0.15, and 0.2:0.2 are found to be very close to each other which indicates that 0.1:0.1 molar ratio is the optimum ratio for the complete formation of CEI on the surface of NMNO cathode. Then, we evaluated the electrochemical stability window of Conv and DS electrolytes. Interestingly, in CV against carbon-coated aluminum (Figure 6A), DS electrolyte exhibited reduced current after 4.0 V (0.772 μA), while Conv electrolyte recorded 1.18 μA after 4.0 V in the 1st cycle (Figure 6B). Even in the 2nd cycle, Conv electrolyte maintained a higher current after 4.0 V, confirming the superior oxidative stability of DS electrolyte. This enhanced anodic stability in DS electrolytes may be attributed to the inclusion of the NaBF_4 additive, which possesses the lowest HOMO level among the 3 anions present in DS electrolytes (shown in Figure 1C). After assessing the electrochemical stability window, we checked the performance of high voltage NMNO cathode in Conv and DS electrolytes, as shown in Figure 6C,D, respectively. Compared to the Conv electrolyte, an enhanced electrochemical performance was observed in the NMNO cathode with the DS electrolyte at a current rate of 0.1 C. This improvement is attributed to reduced electrolyte degradation at higher voltage and the formation of a stable and thin CEI on the

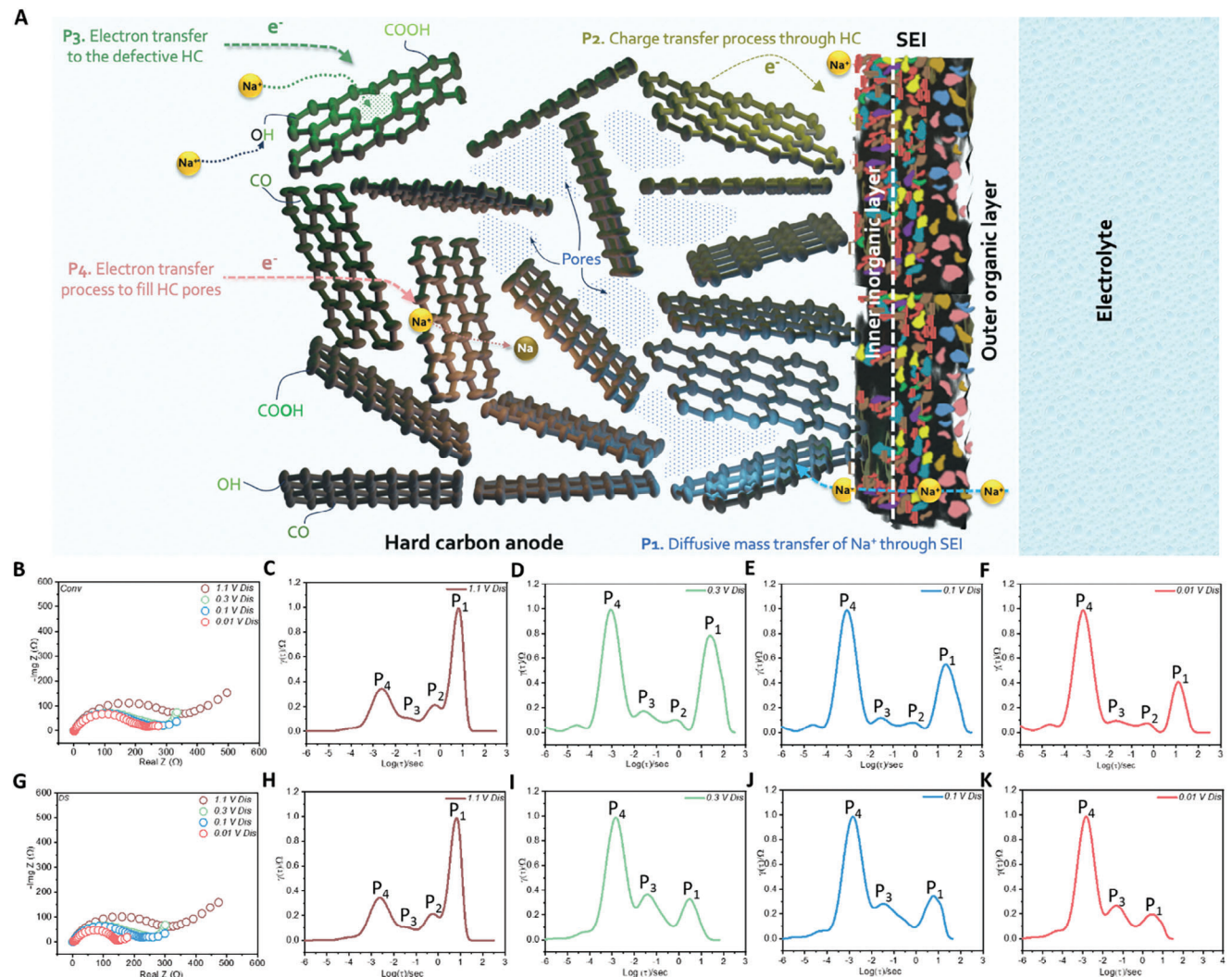


Figure 5. A) Schematic indicating processes P1, P2, P3, and P4; B) Nyquist impedance plot for Char 1100 HC anode in Conv electrolyte at different voltages (1.1, 0.3, 0.1, and 0.01 V) during 1st discharge and their corresponding DRT Plots (C, D, E, and F); G) Nyquist impedance plot for Char 1100 HC anode in DS electrolyte at different voltages (1.1, 0.3, 0.1, and 0.01 V) during 1st discharge and their corresponding DRT Plots (H, I, J, and K).

surface of the NMNO cathode. The 1st charge/discharge capacities for the NMNO cathode in Conv and DS electrolytes were 129.39/119.64 mAh g⁻¹ and 136.11/130.88 mAh g⁻¹, respectively. This results in an ICE of 92.46% and 96.1%, respectively, indicating more electrolyte decomposition reactions in Conv electrolyte when operating the NMNO cathode above 4.2 V. After 200 cycles, the NMNO cathode exhibited capacity retentions of 84.3% and 62.3% in DS and Conv electrolytes. This result strongly underscores the enduring cycling stability of the high-voltage NMNO cathode when paired with DS electrolyte.

To examine the impact of electrolytes on the cycling stability of the NMNO cathode, we analyzed structural alterations of the cathode by acquiring SEM images of the NMNO electrodes extracted from half cells after undergoing 200 cycles in Conv and DS electrolytes. Further, XPS was employed to check the composition of CEI formed on the surface of the NMNO cathode and to detect any possible oxygen evolution in Conv and DS electrolytes. In Figure 6E–H, SEM images depict Pristine NMNO,

NMNO cycled in Conv, and NMNO cycled in DS electrolyte. The Pristine NMNO cathode exhibits a well-defined hexagonal shape (Figure 6E). However, upon cycling in Conv electrolyte, significant cracking, and corrosion of NMNO particles is observed, accompanied by the delamination of the T_mO₂ layers of the NMNO cathode (Figure 6F,G). In contrast, an intact structure with preserved morphology is evident in the case of DS electrolyte (Figure 6H).

Figure S13A–C (Supporting Information) presents the C 1s XPS spectra of pristine NMNO, NMNO cycled in Conv, and NMNO cycled in DS electrolyte. Pristine NMNO exhibits peaks at 284.6 eV (C–C)^[13] and 285.3 eV (C–H)^[13] from conductive carbon and an additional peak at 289.6 eV from the Na₂CO₃.^[58] In contrast, NMNO cycled in Conv electrolyte shows peaks at 284.5 eV (C–C),^[60] 286 eV (C–O),^[59] and 288.7 eV (O–C=O).^[60] NMNO cycled in DS electrolyte shows peaks at 284.3 eV (C–C),^[15] 286 eV (C–O),^[15] 288.8 eV (O–C=O),^[61] and 293.3 eV from the presence of organofluorine (C–F) components^[62,63] on the NMNO surface.

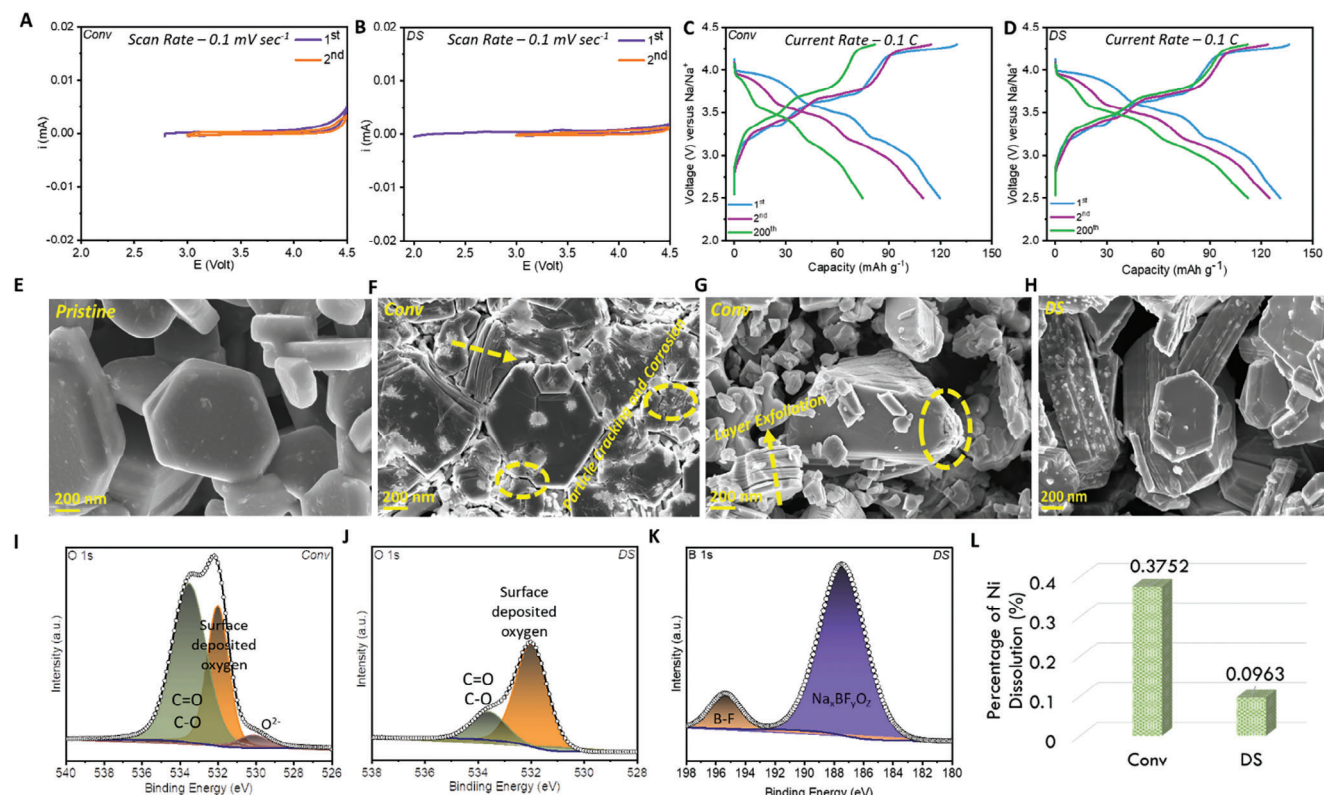


Figure 6. Electrochemical stability window investigated through CV at a scan rate of 0.1 mV sec^{-1} for A) Con and B) DS electrolyte; Galvanostatic profile of NMNO cathode at a current rate of 0.1 C ($1 \text{ C} = 173 \text{ mA g}^{-1}$) in C) Conv and D) DS electrolyte; SEM images of E) Pristine NMNO cathode; F) and G) NMNO cycled in Conv electrolyte for 200 cycles; H) NMNO cycled in DS electrolyte for 200 cycles; O 1s XPS on the surface of I) NMNO cycled in Conv electrolyte for 200 cycles; J) NMNO cycled in DS electrolyte for 200 cycles; K) B 1s XPS on the surface of NMNO cycled in DS electrolyte for 100 cycles; L) Percentage of Ni dissolution investigated through ICP-AES on separator extracted from NMNO/Na half-cell cycled in Conv and DS electrolytes after 200 cycles.

A noticeable increase in C–O and O–C=O components is evident in the Conv electrolyte compared to the DS electrolyte, confirming the greater participation of solvents in the formation of CEI.

Figure S13D–F (Supporting Information) displays F 1s XPS spectra, where pristine NMNO shows a peak at 688 eV coming from the C–F bond from the PVDF binder.^[16] NMNO cycled in Conv electrolyte exhibits peaks at 685.3^[15] and 688.2 eV,^[16] attributed to Na–F and C–F bond formation from PVDF, while NMNO cycled in DS electrolyte shows peaks at 685^[15] and 688.1 eV,^[16] corresponding to Na–F and C–F bond formation from PVDF. The presence of NaF is more pronounced in Conv electrolytes. The structural degradation of the NMNO cathode in the Conv electrolyte is linked to the insulation effect caused by the prevalent presence of NaF and Na₂CO₃ species (identified through XPS) on the NMNO surface. These species result from parasitic reactions at the electrode/electrolyte interphase, further causing the dissolution of transition metal upon interaction with the unstable electrolyte. The insulation effect caused by these NaF and Na₂CO₃ species induces compositional heterogeneity across the cathode after cycling, leading to stresses, distortions in the metal oxide layer, and fractures in the NMNO particles.^[64,65] The formation of NaF and Na₂CO₃ on the surface of the NMNO cathode in the case of DS electrolyte was found to be lesser,

as revealed through F 1s XPS. In contrast, excess NaF and Na₂CO₃ formed on the NMNO cathode in an unstable Conv electrolyte, causing huge fractures and particle corrosion of the NMNO cathode, impeding its long-cycle performance against sodium.^[64]

Additionally, Figure 6I reveals O 1s XPS spectra, indicating T_M–O dissolution at 530.01 eV^[65] in NMNO cycled in Conv electrolyte, absent in NMNO cycled in DS electrolyte (Figure 6J). The presence of carbonate (533.54 eV)^[66] and surface-deposited oxygen species (531.99 eV)^[65] was also significantly reduced in the DS electrolyte compared to the Conv electrolyte. The presence of additional B–O and B–F components (Figure 6K) in the CEI on the surface of the NMNO cathode when cycled in DS electrolyte. These bonds are identified as effective in inhibiting undesired side reactions, forming a protective CEI, preserving the structural integrity of the cathode, and ensuring prolonged cycling performance.

A similar XPS analysis was conducted post-cycling to investigate the composition of the SEI on the Char1100 HC anode, which indicates minimal alteration, as demonstrated by XPS (Figure S14A–F, Supporting Information). Despite undergoing 200 cycles in the DS electrolyte, the Char1100 HC anode's surface continues to exhibit the presence of inorganic components resulting from the reduction of dual anion additives. This persistence confirms the suppression of the SEI dissolution issue

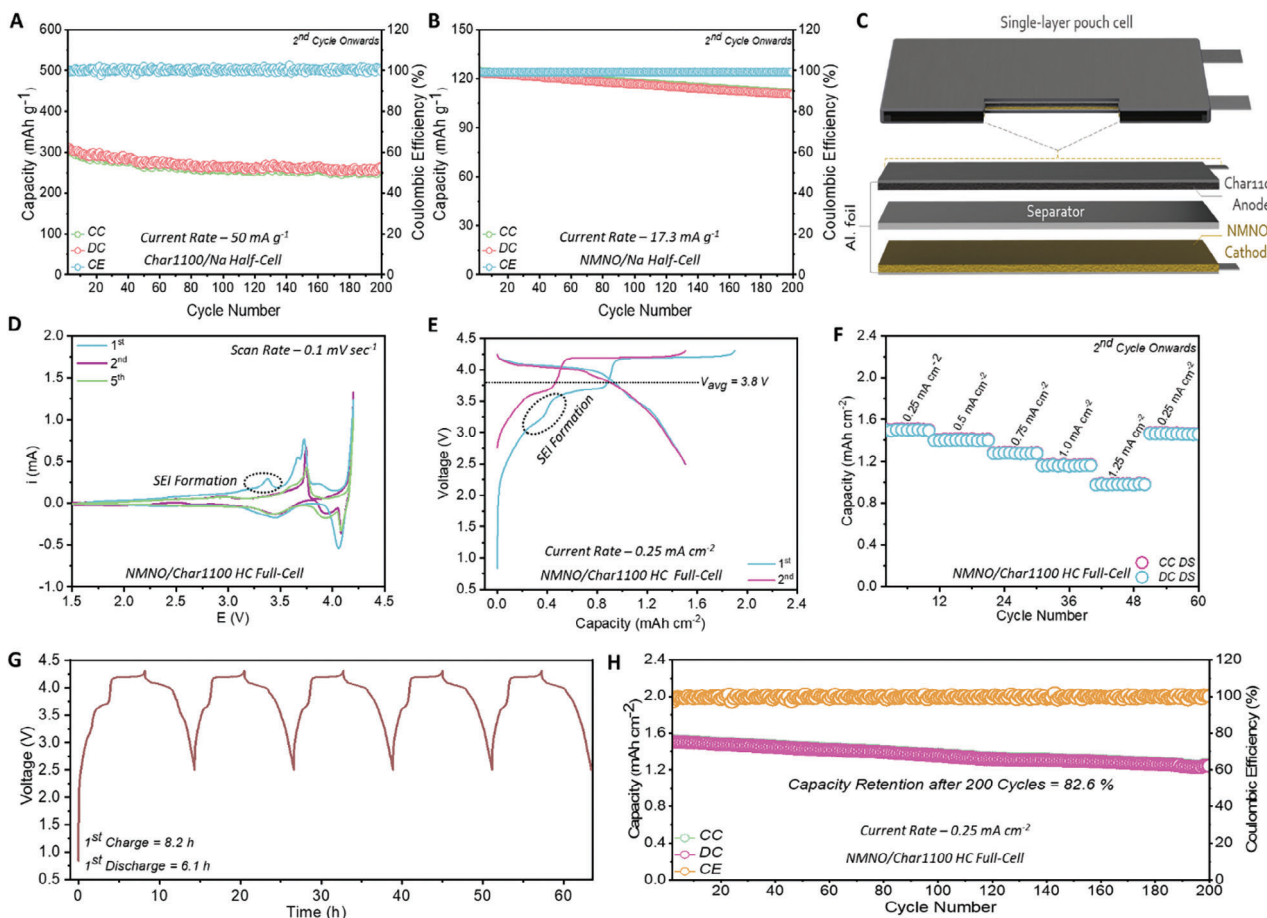


Figure 7. Long cycle performance in DS electrolyte for A) Char1100 HC anode and B) NMNO cathode; C) Schematic of one side coated single-layer pouch cell fabricated using Char1100 HC anode and NMNO cathode; D) CV profile of NMNO/Char1100 pouch cell at a scan rate of 0.1 mV sec^{-1} ; E) Galvanostatic profile of NMNO/Char1100 pouch cell at a current rate of 0.25 mA cm^{-2} ; F) Rate performance of NMNO/Char1100 pouch cell at $0.25, 0.5, 0.75, 1.00$, and 1.25 mA cm^{-2} respectively; G) Voltage versus time profile of NMNO/Char1100 pouch cell H) Long cycling performance of NMNO/Char1100 pouch cell at a current rate of 0.25 mA cm^{-2} .

on the HC electrode, attributed to the inclusion of dual anion additives in the electrolyte system.

We additionally performed an ICP-AES analysis of the separator removed from the NMNO/Na half-cell cycled in the Conv and DS electrolytes after 200 cycles to determine the percentage of Nickel (Ni) dissolution in both electrolytes. Our findings revealed a significantly decreased dissolution of transition metal when NMNO was cycled in DS electrolyte (0.09% of Ni), in contrast to Conv electrolyte (0.37% of Ni), as illustrated in Figure 6L. These findings underscore the role of dual anion additives in mitigating the dissolution of transition metals in the NMNO cathode, thus providing additional support for the enhanced cycling performance observed in the NMNO cathode and Char1100 HC anode.

2.7. Electrochemical Performance of NMNO/Char1100 HC Full-Cell

Following an assessment of the compatibility of DS electrolyte in both the anode (HC) and cathode (NMNO) for long cycle per-

formance as shown in Figure 7A,B, respectively, as well as an investigation into its high voltage stability up to 4.5 V, we constructed one side coated single-layered pouch cell incorporating the Char1100 HC anode and NMNO cathode in DS electrolyte with a balanced mass loading of 5 mg cm^{-2} for HC and 15 mg cm^{-2} for NMNO respectively (schematic is shown in Figure 7C). The CV profile of the NMNO/Char1100 HC full cell at a scan rate of 0.1 mV sec^{-1} (Figure 7D) exhibits overlapping peaks from the 1st to the 5th cycle, confirming the reversible storage of Na^+ ions in the cathode against the Char1100 HC anode in sodium ion full cell. Except for CV peaks above 3.5 V corresponding to $\text{Ni}^{2+}/\text{Ni}^{3+}$ redox, we found an additional peak at 3.3 V in the 1st cycle, which disappeared from the 2nd cycle onward. We attribute this peak to the SEI formation on the Char1100 HC anode. The galvanostatic charge-discharge profile of the pouch cell at a current rate of 0.25 mA cm^{-2} yielded a 1st charge/discharge capacity of $1.89/1.50 \text{ mAh cm}^{-2}$, with an excellent ICE of $\approx 79\%$ (Figure 7E). The formation of the SEI during the first sodiation of Char1100 was also observed at $\approx 3.3 \text{ V}$ in the charge-discharge profile, which has been highlighted in Figure 7E. The rate capability of the pouch cell was further investigated by charging and

discharging the cell at various current rates (0.25, 0.5, 0.75, 1.00, and 1.25 mA cm⁻²), as shown in Figure 7F. The cell exhibits an excellent rate capability of 0.98 mA cm⁻² even at a high current rate of 1.25 mA cm⁻². This suggests that the interfaces developed on both the anode and cathode in the sodium-ion full cell are effectively facilitating the diffusion of Na⁺ ions across these interfaces.

Figure 7G illustrates the voltage versus time profile of the NMNO/Char1100 HC full cell. During its initial charge, the cell takes 8.2 h, while its discharge lasts 6.1 h, both occurring at a current rate of 0.25 mA cm⁻². Subsequent cycles show consistent charge and discharge times of \approx 6 h, as depicted in Figure 7G. The pouch cell demonstrated remarkable capacity retention of 82.6% after 200 cycles at a current rate of 0.25 mA cm⁻², showcasing outstanding stability for a large-scale format sodium ion battery pouch cell, as shown in Figure 7H.

In summary, the remarkable performance of the NMNO/Char1100 HC sodium full cell can be ascribed to several enhancements resulting from the incorporation of dual anion additives. These include improvements in the SEI composition and a reduction in SEI dissolution. Additionally, there are advancements in the electrochemical stability window and an enhancement in the chemical stability of the CEI on the high-voltage NMNO cathode.

3. Conclusion

In conclusion, our work introduces an innovative method for regulating the inner solvation structure of carbonate electrolytes by incorporating higher donor number dual anion additives (BF₄⁻ and TFSI⁻) into the conventional electrolyte system (1 M NaPF₆ EC:PC). The inclusion of these additives results in a notable enhancement of ICE in the Char1100 HC anode from 39% to 78%, alongside the promotion of inorganic-rich SEI and CEI on the surface of the Char1100 HC anode and high voltage NMNO oxide-based cathode, respectively. Our findings, supported by DFT and MD simulation calculations, confirm the active participation of dual anion additives in the inner solvation shell around the Na⁺ cation, influencing the reductive stability of the pure solvent molecules and Na⁺-solvent complex by raising their LUMO levels upon the introduction of anions as compared to the LUMO level of Na⁺-solvent-anion complexes in the electrolyte system. The improved reductive stability of the solvents was seen in the CV profile of Char1100 HC, where a delayed reduction confirmed by the shifting of the reduction peak at 1.0 V to a lower voltage value of 0.7 V was observed, which helped in the formation of a homogenous and inorganic components rich anion derived SEI on the surface of Char1100 HC anode. The composition of the derived SEI was revealed by the combination of XPS, HR-TEM, and TOF-SIMS analysis. The presence of inorganic fragments coming from the decomposition of dual anions identified in the TOF-SIMS mass spectra strongly supported our hypothesis regarding the modification of the solvation structure around the Na⁺ cation upon adding dual anion additives.

The inorganic-rich SEI on the Char1100 HC anode enhances ICE. It exhibits improved rate capability due to enhanced diffusion kinetics, as confirmed by Randles Sevcik's equation, DRT, and desolvation energy calculations using FEP methods. The inorganic-rich CEI on the NMNO cathode surface mitigates in-

sulative sodium carbonate formation and transition metal dissolution alongside suppressing the structural degradations, contributing to enhanced long-term cycling performance in sodium batteries.

Moreover, the single-layered pouch cell, integrating the Char1100 HC anode and NMNO cathode in an electrolyte with dual anion additive added electrolyte, showcased promising characteristics. It exhibited an ICE of \approx 79% and the ability to deliver an areal capacity of 1.5 mAh cm⁻² at a current rate of 0.25 mA cm⁻². Even after 200 cycles, it retained 82.6% of its initial discharge capacity. Our findings emphasize the considerable promise of our novel electrolyte engineering strategy in enhancing both the high voltage capabilities and long-term cycling efficiency of sodium-ion battery systems. This suggests an avenue for further investigation into the electrolyte components to improve the electrochemical performance of these battery systems. The electrolyte engineering method detailed in this study provides a pathway for advancing high-voltage next-generation sodium-ion batteries.

4. Experimental Section

Resource Availability: **Lead Contact:** Further information and requests for resources and materials should be directed to and will be fulfilled by the Lead Contact, Sagar Mitra (sagar.mittra@iitb.ac.in).

Materials Availability: This study did not generate new unique materials.

Data and Code Availability: The published article encompasses all datasets and results derived or scrutinized throughout this study. Although the datasets and results supporting the current study have not been deposited in a public repository, they can be obtained from the Lead Contact upon request.

Supporting Information

Supporting Information is available from the Wiley Online Library or from the author.

Acknowledgements

The authors acknowledge the instrumental facilities provided by the Sophisticated Analytical Instrument Facility (SAIF), IRCC (IIT Bombay, India), and National Centre for Photovoltaic Research and Education (NCPRE), IIT Bombay. The authors are thankful for the financial support provided by DST-SERB, the Government of India (Grant No. IPA/2021/000048). The author would also like to extend their acknowledgement for accessing the facility of TOF-SIMS at the Central Research Facility, Indian Institute of Technology, Delhi, Sonipat Campus.

Conflict of Interest

The authors declare no competing interests.

Author Contributions

H.L. and A.K. contributed equally to this work. H.L. and A.K. designed the research framework, carried out the experiments, and drafted the manuscript. A.B. performed MD simulations. A.G. performed DFT calculations. H.L., A.K., A.B., A.G., P.K., A.A., A.S., D.T.M., and S.M. contributed

to data curation, writing, and editing. D.K. performed the DRT. All authors discussed the results extensively during this research work. S.M. supervised and helped in designing the work received financial assistance, and edited the manuscript. All authors discussed the work and gave the final form.

Data Availability Statement

The data that support the findings of this study are available from the corresponding author upon reasonable request.

Keywords

Dual anion additive, electrolyte engineering, High voltage cathode, Primary solvation shell modification, sodium-ion battery

Received: March 20, 2024

Revised: May 5, 2024

Published online: May 28, 2024

- [1] W. Ren, Z. Zhu, Q. An, L. Mai, *Small* **2017**, *13*, 1604181.
- [2] Y. Huang, L. Zhao, L. Li, M. Xie, F. Wu, R. Chen, *Adv. Mater.* **2019**, *31*, 1808393.
- [3] M. Zhang, Y. Li, F. Wu, Y. Bai, C. Wu, *Nano Energy* **2021**, *82*, 105738.
- [4] H. Xie, Z. Wu, Z. Wang, N. Qin, Y. Li, Y. Cao, Z. Lu, *J. Mater. Chem. A Mater.* **2020**, *8*, 3606.
- [5] Y. You, A. Manthiram, *Adv. Energy Mater.* **2018**, *8*, 1701785.
- [6] M. Ma, H. Cai, C. Xu, R. Huang, S. Wang, H. Pan, Y. S. Hu, *Adv. Funct. Mater.* **2021**, *31*, 2100278.
- [7] Y. Wan, Y. Liu, D. Chao, W. Li, D. Zhao, *Nano. Mater. Sci.* **2022**, *5*, 189.
- [8] K. Fang, Y. Tang, J. Liu, Z. Sun, X. Wang, L. Chen, X. Wu, Q. Zhang, L. Zhang, Y. Qiao, S. G. Sun, *Nano Lett.* **2023**, *23*, 6681.
- [9] B. Peng, Z. Sun, L. Zhao, S. Zeng, G. Zhang, *Batter Supercaps* **2021**, *4*, 456.
- [10] H. Yuan, F. Ma, X. Wei, J. Le Lan, Y. Liu, Y. Yu, X. Yang, H. S. Park, *Adv. Energy Mater.* **2020**, *10*, 2001418.
- [11] M. Liu, J. Zhang, S. Guo, B. Wang, Y. Shen, *ACS Appl. Mater. Interfaces* **2020**, *15*, 17620.
- [12] X. Liu, Y. Tan, T. Liu, W. Wang, C. Li, J. Lu, Y. Sun, *Adv. Funct. Mater.* **2019**, *29*, 1.
- [13] S. Komaba, W. Murata, T. Ishikawa, N. Yabuuchi, T. Ozeki, T. Nakayama, A. Ogata, K. Gotoh, K. Fujiwara, *Adv. Funct. Mater.* **2011**, *21*, 3859.
- [14] J. H. Jo, J. U. Choi, Y. J. Park, J. K. Ko, H. Yashiro, S. T. Myung, *Energy Storage Mater.* **2020**, *32*, 281.
- [15] H. Lohani, A. Kumar, P. Kumari, A. Ahuja, M. Gautam, A. Sengupta, S. Mitra, *ACS Appl. Mater. Interfaces* **2022**, *14*, 37793.
- [16] I. Moezz, D. Susanto, W. Chang, H. D. Lim, K. Y. Chung, *Chem. Eng. J.* **2021**, *425*, 130547.
- [17] Y. J. Chang, G. H. Xie, Y. M. Zhou, J. X. Wang, Z. X. Wang, H. J. Guo, B. Z. You, G. C. Yan, *Transact. Norferr. Metals Soc. China* **2022**, *32*, 262.
- [18] H. Lu, X. Chen, Y. Jia, H. Chen, Y. Wang, X. Ai, H. Yang, Y. Cao, *Nano Energy* **2019**, *64*, 103903.
- [19] Y. S. Hu, H. Pan, A. C. S. *Energy Lett.* **2022**, *7*, 4501.
- [20] Z. Tian, Y. Zou, G. Liu, Y. Wang, J. Yin, J. Ming, H. N. Alshareef, *Adv. Sci.* **2022**, *9*, 2201207.
- [21] Y. Lee, J. Lee, H. Kim, K. Kang, N. S. Choi, *J. Power Sources* **2016**, *320*, 49.
- [22] T. Nakano, N. Yabuuchi, S. Fujimura, J. Son, Y. Cui, H. Oji, S. Komaba, *ChemElectroChem* **2016**, *3*, 1856.
- [23] H. J. Liang, Z. Y. Gu, X. X. Zhao, J. Z. Guo, J. L. Yang, W. H. Li, B. Li, Z. M. Liu, W. L. Li, X. L. Wu, *Angew. Chem. Int. Ed.* **2021**, *60*, 26837.
- [24] Y. Li, F. Wu, Y. Li, M. Liu, X. Feng, Y. Bai, C. Wu, *Chem. Soc. Rev.* **2022**, *51*, 4484.
- [25] N. Yao, S. Y. Sun, X. Chen, X. Q. Zhang, X. Shen, Z. H. Fu, R. Zhang, Q. Zhang, *Angew. Chem. Int. Ed.* **2022**, *61*, 2210859.
- [26] G. Zhang, L. Zhang, Q. Ren, L. Yan, F. Zhang, W. Lv, Z. Shi, *ACS Appl. Mater. Interfaces* **2021**, *13*, 31650.
- [27] S. Alvin, D. Yoon, C. Chandra, H. S. Cahyadi, J. H. Park, W. Chang, K. Y. Chung, J. Kim, *Carbon N Y* **2019**, *145*, 67.
- [28] H. Xiang, D. Mei, P. Yan, P. Bhattacharya, S. D. Burton, A. Von Wald Cresce, R. Cao, M. H. Engelhard, M. E. Bowden, Z. Zhu, B. J. Polzin, C. M. Wang, K. Xu, J. G. Zhang, W. Xu, *ACS Appl. Mater. Interfaces* **2015**, *7*, 20687.
- [29] P. Desai, J. Forero-Saboya, V. Meunier, G. Rousse, M. Deschamps, A. M. Abakumov, J. M. Tarascon, S. Mariyappan, *Energy Storage Mater.* **2023**, *57*, 102.
- [30] A. Ponrouch, E. Marchante, M. County, J. M. Tarascon, M. R. Palacín, *Energy Environ. Sci.* **2012**, *5*, 8572.
- [31] X. Liu, L. Fang, X. Lyu, R. E. Winans, T. Li, *Chem. Mater.* **2023**, *35*, 9821.
- [32] Z. Yu, Z. Shi, S. R. Bheemireddy, E. Kamphaus, X. Lyu, M. A. Uddin, Z. Li, Z. Yang, T. Li, J. S. Moore, L. Zhang, L. Cheng, *J. Mater. Chem. A Mater.* **2024**, *12*, 6294.
- [33] Y. Zhang, N. H. C. Lewis, J. Mars, G. Wan, N. J. Weadock, C. J. Takacs, M. R. Lukatskaya, H. G. Steinrück, M. F. Toney, A. Tokmakoff, E. J. Maginn, *J. Phys. Chem. B* **2021**, *125*, 4501.
- [34] K. Qian, R. E. Winans, T. Li, *Adv. Energy Mater.* **2021**, *11*, 2002821.
- [35] X. Lyu, H. Wang, X. Liu, L. He, C. Do, S. Seifert, R. E. Winans, L. Cheng, T. Li, *ACS Nano* **2024**, *18*, 7037.
- [36] J. Lim, K. Park, H. Lee, J. Kim, K. Kwak, M. Cho, *J. Am. Chem. Soc.* **2018**, *140*, 15661.
- [37] X. Liu, S. C. Lee, S. Seifer, R. E. Winans, L. Cheng, Y. Z. T. Li, *Energy Storage Mater.* **2022**, *45*, 696.
- [38] Y. Zhang, E. J. Maginn, *J. Phys. Chem. B* **2021**, *125*, 13246.
- [39] A. Xiao, B. Lucht, L. Yang, S. Kang, D. Abraham, *ECS Trans.* **2009**, *16*, 141.
- [40] X. Wang, Z. Song, H. Wu, H. Yu, W. Feng, M. Armand, X. Huang, Z. Zhou, H. Zhang, *Angew. Chem. Int. Ed.* **2022**, *61*, 2211623.
- [41] S. A. M. Noor, N. C. Su, L. T. Khoon, N. S. Mohamed, A. Ahmad, M. Z. A. Yahya, H. Zhu, M. Forsyth, D. R. MacFarlane, *Electrochim. Acta* **2017**, *247*, 983.
- [42] F. Cheng, M. Cao, Q. Li, C. Fang, J. Han, Y. Huang, *ACS Nano* **2023**, *17*, 18608.
- [43] J. Forero-Saboya, P. Desai, R. Healy Corominas, E. Raymundo-Piñero, A. Canizares, D. Foix, J.-M. Tarascon, S. Mariyappan, *J. Electrochem. Soc.* **2023**, *170*, 100529.
- [44] D. Monti, E. Jónsson, A. Boschin, M. R. Palacín, A. Ponrouch, P. Johansson, *Phys. Chem. Chem. Phys.* **2020**, *22*, 22768.
- [45] O. Zavorotynska, M. Corno, A. Damin, G. Spoto, P. Ugliengo, M. Baricco, *J. Phys. Chem. C* **2011**, *115*, 18890.
- [46] S. Sankarasubramanian, J. Kahky, V. Ramani, *Proc. Natl. Acad. Sci. U.S.A.* **2019**, *116*, 14899.
- [47] Y. Lin, X. Jin, S. Gao, F. Liu, S. Huang, X. Yang, Y. Chen, Y. Meng, *Chem. A Eur. J.* **2024**, 2303741.
- [48] G. G. Eshetu, T. Diemant, M. Hekmatfar, S. Grugeon, R. J. Behm, S. Laruelle, M. Armand, S. Passerini, *Nano Energy* **2019**, *55*, 327.
- [49] Y. Pan, Y. Zhang, B. S. Parimalam, C. C. Nguyen, G. Wang, B. L. Lucht, *J. Electroanal. Chem.* **2017**, *799*, 181.
- [50] M. Dahbi, T. Nakano, N. Yabuuchi, S. Fujimura, K. Chihara, K. Kubota, J. Y. Son, Y. T. Cui, H. Oji, S. Komaba, *ChemElectroChem* **2016**, *3*, 1856.
- [51] Z. Cao, X. Zheng, Y. Wang, W. Huang, Y. Li, Y. Huang, H. Zheng, *Nano Energy* **2022**, *93*, 106811.
- [52] S. Wang, Y. Chen, Y. Jie, S. Lang, J. Song, Z. Lei, S. Wang, X. Ren, D. Wang, X. Li, R. Cao, G. Zhang, S. Jiao, *Small Methods* **2020**, *4*, 1900856.

- [53] J. Sun, L. A. O'Dell, M. Armand, P. C. Howlett, M. Forsyth, *ACS Energy Lett.* **2021**, *6*, 2481.
- [54] B. Sayahpour, W. Li, S. Bai, B. Lu, B. Han, Y.-T. Chen, G. Deysher, S. Parab, P. Ridley, G. Raghavendran, L. H. B. Nguyen, M. Zhang, Y. S. Meng, *Energy Environ. Sci.* **2024**, *12*, 1216.
- [55] D. Morales, L. G. Chagas, D. Paterno, S. Greenbaum, S. Passerini, S. Suarez, *Electrochim. Acta* **2021**, *377*, 138062.
- [56] R. Tatara, Y. Okamoto, Y. Ugata, K. Ueno, M. W atanabe, K. Dokko, *Electrochemistry* **2021**, *89*, 590.
- [57] K. Schutjajew, T. Tichter, J. Schneider, M. Antonietti, C. Roth, M. Oschatz, *Phys. Chem. Chem. Phys.* **2021**, *23*, 11488.
- [58] L. Dai, Z. Guo, Z. Wang, S. Xu, S. Wang, W. Li, G. Zhang, Y. J. Cheng, Y. Xia, *Small* **2023**.
- [59] P. Thomas, D. Billaud, *Electrochim. Acta* **2002**, *47*, 3303.
- [60] M. Chen, W. Hua, J. Xiao, D. Cortie, W. Chen, E. Wang, Z. Hu, Q. Gu, X. Wang, S. Indris, S. L. Chou, S. X. Dou, *Nat. Commun.* **2019**, *10*.
- [61] A. Ponrouch, R. Dedryvère, D. Monti, A. E. Demet, J. M. Ateba Mba, L. Croguennec, C. Masquelier, P. Johansson, M. R. Palacín, *Energy Environ. Sci.* **2013**, *6*, 2361.
- [62] G. Nansé, E. Papirer, P. Fioux, F. Moguet, A. Tressaud, *Carbon N Y* **1997**, *35*, 175.
- [63] G. M. Veith, M. Doucet, R. L. Sacci, B. Vacaliuc, J. K. Baldwin, J. F. Browning, *Sci. Rep.* **2017**, *7*, 6326.
- [64] D. DiLecce, V. Marangon, M. Isaacs, R. Palgrave, P. R. Shearing, J. Hassoun, *Small Methods* **2021**, *5*.
- [65] W. Zuo, A. Innocenti, M. Zarzabeitia, D. Bresser, Y. Yang, S. Passerini, *Acc. Chem. Res.* **2023**, *56*, 284.
- [66] X. Cao, H. Li, Y. Qiao, X. Li, M. Jia, J. Cabana, H. Zhou, *Adv. Energy Mater.* **2020**, *10*.